



HAL
open science

Rheology of three-dimensional packings of aggregates: Microstructure and effects of nonconvexity

Emilien Azéma, Farhang Radjai, Baptiste Saint-Cyr, Jean-Yves Delenne,
Philippe Sornay

► **To cite this version:**

Emilien Azéma, Farhang Radjai, Baptiste Saint-Cyr, Jean-Yves Delenne, Philippe Sornay. Rheology of three-dimensional packings of aggregates: Microstructure and effects of nonconvexity. *Physical Review E: Statistical, Nonlinear, and Soft Matter Physics*, 2013, 87 (052205), pp.1-15. 10.1103/PhysRevE.87.052205 . hal-00826186

HAL Id: hal-00826186

<https://hal.science/hal-00826186v1>

Submitted on 27 May 2013

HAL is a multi-disciplinary open access archive for the deposit and dissemination of scientific research documents, whether they are published or not. The documents may come from teaching and research institutions in France or abroad, or from public or private research centers.

L'archive ouverte pluridisciplinaire **HAL**, est destinée au dépôt et à la diffusion de documents scientifiques de niveau recherche, publiés ou non, émanant des établissements d'enseignement et de recherche français ou étrangers, des laboratoires publics ou privés.

Emilien Azéma,^{1,*} Farhang Radjai,^{1,†} Baptiste Saint-Cyr,^{1,2} Jean-Yves Delenne,³ and Philippe Sornay²

¹*Université Montpellier 2, CNRS, LMGC, Cc 048,*

Place Eugène Bataillon, F-34095 Montpellier cedex 05, France

²*CEA, DEN, DEC, SPUA, LCU, F-13108 St Paul lez Durance, (France)*

³*IATE, UMR 1208 INRA-CIRAD-Montpellier Supagro-UM2,*

2 place Pierre Viala, F-34060 Montpellier cedex 01, France.

(Dated: May 4, 2013)

We use 3D contact dynamics simulations to analyze the rheological properties of granular materials composed of rigid aggregates. The aggregates are made from four overlapping spheres and described by a nonconvexity parameter depending on the relative positions of the spheres. The macroscopic and microstructural properties of several sheared packings are analyzed as a function of the degree of nonconvexity of the aggregates. We find that the internal angle of friction increases with nonconvexity. In contrast, the packing fraction increases first to a maximum value but declines as nonconvexity further increases. At high level of nonconvexity, the packings are looser but show a higher shear strength. At the microscopic scale, the fabric and force anisotropy, as well as friction mobilization are enhanced by multiple contacts between aggregates and interlocking, revealing thus the mechanical and geometrical origins of shear strength.

I. INTRODUCTION

Particle shape is a major parameter for the rheological properties of granular materials such as their shear strength, flowability and packing structure. However, recent research has mostly focussed on the complex rheology and micromechanical properties of granular materials by considering simple shapes such as disks and spherical particles. More realistic materials composed of nonspherical particles now begin to be investigated by experiments and discrete element numerical simulations [1–14]. This interest is motivated by new challenges in civil engineering and powder technology where most processes need to be optimized or revised following the dramatic degradation of natural resources [5, 10, 15–19]. Realistic particle shapes raise also fundamental issues. In particular, it is essential to understand to which extent our present understanding of the rheology of granular materials based on model packings can be extended to complex granular materials for the understanding of the behavior and primary mechanisms at the natural scale of particles and their interactions.

Most granular materials are found with particles of various degrees of sphericity, elongation, angularity, facetedness and convexity. A general observation is that angular and elongated particles present a higher shear strength than spherical particles [8, 11, 19–24]. But only recently it was evidenced by systematic simulations that the shear strength is an increasing linear function of elongation [25, 26] whereas it increases first with particle angularity up to a maximum value and then saturates as the particles become more angular [27, 28]. In contrast, the packing fraction varies unmonotonically with elongation as for

example in packings of ellipsoidal shapes [4, 25, 29–31]. In all reported cases, the networks resulting from various shapes appear to be complex and hardly amenable to simple statistical modeling.

A systematic study is now possible not only due to the available computer power and memory, required for contact detection algorithms between complex shapes [23, 32–34], but also because recent investigations have shown that simple parameters can be defined to generate particle shapes with continuously-variable shape parameters. Among others, the shape parameter η describing the degree of distortion from a perfectly circular or spherical shape was used successfully recently in 2D to analyze several packings composed of elongated (rounded-cap rectangles) [25, 35], angular (irregular hexahedra) [26], and nonconvex shapes (aggregates of overlapped disks)[36, 37]. The shear strength and packing fraction for all those particle shapes are mainly controlled by η so that the effect of the parameters specific to each shape (angularity, nonconvexity, elongation) may be considered to be of second order as compared to η [38].

In this paper, we investigate granular materials composed of nonconvex particles in three dimensions. Nonconvex particles are of special interest because the collective behavior of such particles has only been studied in two dimensions [36, 37, 39] and also because they give a rise to a rich microstructure where a pair of particles can interact at several contact points (multiple contacts), leading to the possibility of interlocking between particles. The nonconvexity may affect the behavior through various mechanisms such as the resulting microstructure (contact network and compactness), hindrance of particle rotations due to interlocking, enhanced mobilization of friction and multiple contacts between particles with an effect similar to that of face-face contacts between angular particles [22, 27, 28, 40].

We consider rigid aggregates of four overlapping spheres with a four-fold rotational symmetry; see Fig.

*Electronic address: emilien.azema@univ-montp2.fr

†Electronic address: franck.radjai@univ-montp2.fr

1. Their nonconvexity can be tuned by adjusting the overlap, the range of shapes varying thus from a sphere for a full overlap of the four spheres, to an aggregate of four tangent spheres. We focus on the quasistatic behavior and analyze the underlying microstructure with increasing level of nonconvexity. We also compare our data with two-dimensional results for aggregates of three overlapped disks.

In the following, we first introduce in sect II the technical details of the simulations and procedures of sample preparation. In section III we present the evolution of shear stress and packing fraction with shear strain and at an increasing level of nonconvexity. The sections IV and V, are devoted to the analysis of contact network topology, force distributions, friction mobilization and force-contact anisotropy. We conclude with a discussion of the most salient results of this work.

II. MODEL DESCRIPTION

The simulations were carried out by means of the contact dynamics (CD) method [41–43]. The CD method is a discrete element approach for the simulation of non-smooth granular dynamics with contact laws expressing mutual exclusion and dry friction between particles and an implicit time integration scheme. Hence, this method is numerically unconditionally stable and particularly adapted for the simulation of frictional contacts between particles. It has been extensively employed for the simulation of granular materials in 2D and 3D [5, 10, 11, 22, 24, 25, 27, 35, 44–51]

The particles are regular aggregates of 4-fold rotational symmetry composed of four overlapping spheres of the same radius r as shown in Fig. 1. This shape can be easily characterized by the ratio $\lambda = l/2r$, where l is the distance between the centers of spheres. This parameter varies from 0, corresponding to a sphere, to $\sqrt{3}/2$ corresponding to an aggregate where three coplanar spheres intersect at a single point, so that the radius R of the circumscribing sphere is given by $R = r(1 + \lambda\sqrt{3}/2)$.

The aggregates may also be characterized by their non-convexity, i.e. their degree of distortion η from a perfectly spherical shape, defined as [25, 35, 38]:

$$\eta = \frac{\Delta R}{R}, \quad (1)$$

where, $\Delta R = R - R'$ and R' the radius of the inscribed circle. ΔR can be seen as the concavity of the aggregate. The parameter η has been used to analyze the effect of particle shape on the quasistatic rheological parameters of assemblies of elongated, angular and non-convex particles in 2D [25, 26, 35–38] as well as for platy particles in 3D [52].

We prepared 8 different packings of 12,000 aggregates with η varying from 0 to 0.7 by steps of 0.1. In order to avoid long-range ordering in the limit of small values of η , we introduce a size polydispersity by taking R in the

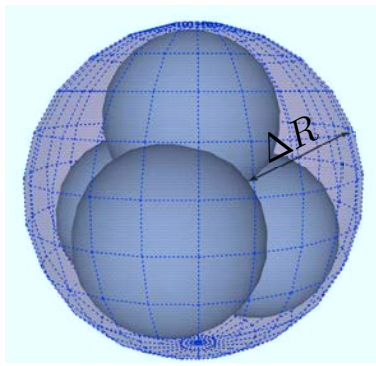


FIG. 1: (Color Online) Geometry of regular aggregate.

range $[R_{min}, R_{max}]$ with $R_{max} = 3R_{min}$ with a uniform distribution in particle volume fractions, which leads to a high packing fraction.

A dense packing composed of spheres is first constructed by means of a layer-by-layer deposition model based on simple geometrical rules [53]. The particles are deposited sequentially on a substrate. For others values of η , the same packing is used with each sphere serving as the circumscribing sphere of aggregates. The aggregates are inscribed with the given value of η and random orientation in the sphere.

Following this geometrical process, each packing is compacted by isotropic compression inside a box of dimensions $L_0 \times l_0 \times H_0$ in which the left, bottom and back walls are fixed and the top, right and front walls are subjected to the same compressive stress σ_0 ; see Fig.2(a). The gravity g and the friction coefficient between particles and with the walls are set to zero during the compression in order to obtain isotropic dense packings.

The isotropic samples are then subjected to vertical compression by downward displacement of the top wall at a constant velocity v_z for a constant confining stress σ_0 acting on the side walls. This is illustrated in figure 2(b) at 15% of vertical displacement of the upper wall. The friction coefficient between particles is set to 0.4 and to zero with the walls. Since we are interested in quasistatic behavior, the shear rate should be such that the kinetic energy supplied by shearing is negligible compared to the static pressure. This can be formulated in terms of an inertia parameter I defined by [54]:

$$I = \dot{\epsilon} \sqrt{\frac{m}{d\sigma_0}}, \quad (2)$$

where $\dot{\epsilon} = v_z/z$ and m is the mean particle mass. The rate-independent regime, corresponding to a quasi-static behavior is characterized by $I < 10^{-3}$, which is the case in our simulations. Note that video samples of the simulations analyzed in this paper can be found following this link : www.cgp-gateway.org/Video/ref022.

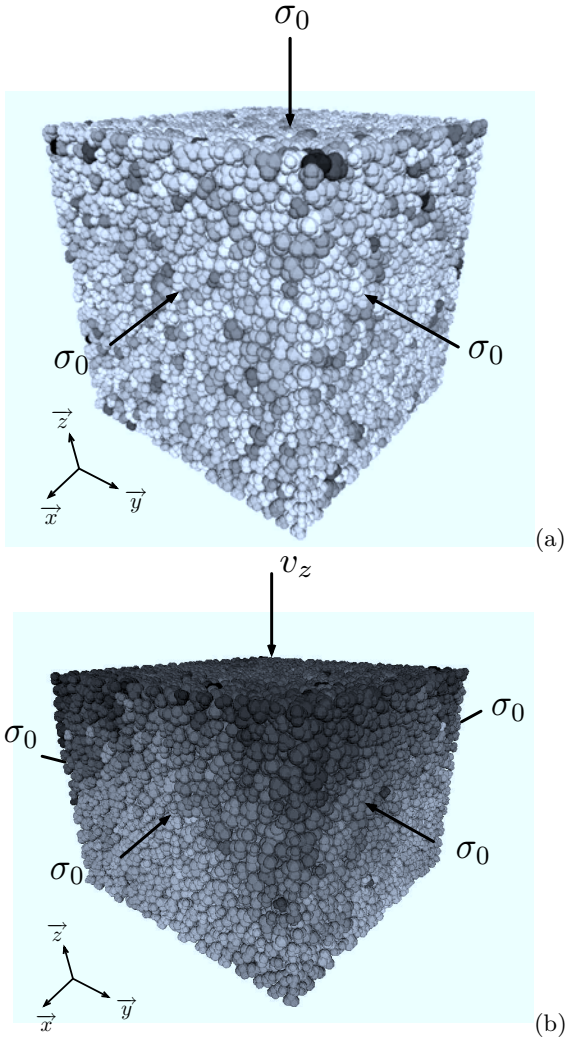


FIG. 2: Boundary conditions for (a) isotropic and (b) triaxial compaction. The grey levels are proportional to particle pressures in (a) and to particle velocities in (b) at $\varepsilon_q = 0.15$.

III. MACROSCOPIC BEHAVIOR

A. Definition of macroscopic parameters

In numerical simulations, the stress tensor can be evaluated from the contact forces and geometrical configuration of the packing. Based on virtual power formalism, an “internal moment” \mathbf{M} can be defined for each particle i [41]:

$$M_{\alpha\beta}^i = \sum_{c \in i} f_{\alpha}^c r_{\beta}^c, \quad (3)$$

where f_{α}^c is the α component of the force exerted on particle i at the contact c , r_{β}^c is the β component of the position vector of the same contact c , and the summation runs over all contact neighbors of particle i (noted briefly by $c \in i$). Then, it can be shown that the internal moment of a collection of rigid particles is the sum of the

internal moments of individual particles, and the stress tensor $\boldsymbol{\sigma}$ in a given volume V is simply the density of the internal moment [41, 48]:

$$\boldsymbol{\sigma} = \frac{1}{V} \sum_{i \in V} \mathbf{M}^i = \frac{1}{V} \sum_{c \in V} f_{\alpha}^c \ell_{\beta}^c, \quad (4)$$

where ℓ^c is the branch vector joining the centers of the two touching particles at the contact point c . Remark that the first summation runs over all particles whereas the second summation runs over the contacts (each contact appearing once).

Under triaxial conditions with vertical compression, we have $\sigma_1 \geq \sigma_2 = \sigma_3$, where the σ_{α} are the stress principal values. The mean stress p and stress deviator q are defined by:

$$p = (\sigma_1 + \sigma_2 + \sigma_3)/3, \quad (5)$$

$$q = (\sigma_1 - \sigma_3)/3. \quad (6)$$

For our system of perfectly rigid particles, the stress state is characterized by the mean stress p and the normalized shear stress q/p .

The cumulative strain components ε_{α} are defined by

$$\varepsilon_1 = \int_{H_0}^H \frac{dH'}{H'} = \ln \left(1 + \frac{\Delta H}{H_0} \right), \quad (7)$$

$$\varepsilon_2 = \int_{L_0}^L \frac{dL'}{L'} = \ln \left(1 + \frac{\Delta L}{L_0} \right), \quad (8)$$

$$\varepsilon_3 = \int_{l_0}^l \frac{dl'}{l'} = \ln \left(1 + \frac{\Delta l}{l_0} \right), \quad (9)$$

where H_0 , l_0 and L_0 are the initial height, width and length of the simulation box, respectively and $\Delta H = H_0 - H$, $\Delta l = l_0 - l$ and $\Delta L = L_0 - L$ are the corresponding cumulative displacements. The volumetric strain is given by

$$\varepsilon_p = \varepsilon_1 + \varepsilon_2 + \varepsilon_3 = \int_{V_0}^V \frac{dV'}{V'} = \ln \left(1 + \frac{\Delta V}{V_0} \right), \quad (10)$$

where V_0 is the initial volume and $\Delta V = V - V_0$ is the total volume change. The cumulative shear strain is defined by

$$\varepsilon_q \equiv \varepsilon_1 - \varepsilon_3. \quad (11)$$

We note that the choice of the deviatoric stress variable q in eq. (6) with a prefactor $1/3$ results from the requirement that the total power $\dot{W} = \sigma_1 \dot{\varepsilon}_1 + \sigma_2 \dot{\varepsilon}_2 + \sigma_3 \dot{\varepsilon}_3$ should be expressed as a sum of the products of the volumetric and deviatoric conjugate variables $\dot{W} = p \dot{\varepsilon}_p + 2 q \dot{\varepsilon}_q$.

B. Shear strength

Figure 3 displays the normalized shear stress q/p as a function of ε_q for all values of η . Due to the initial

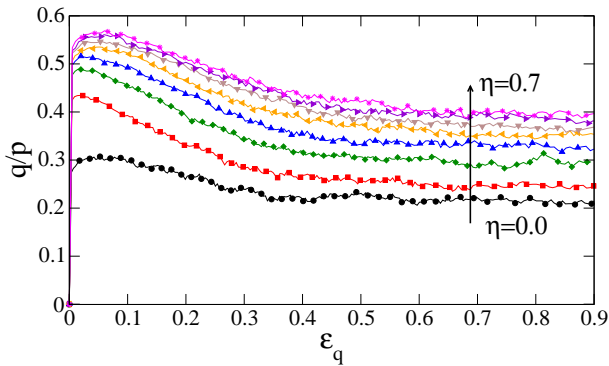


FIG. 3: (Color Online) Normalized shear stress q/p as a function of the cumulative shear strain ε_q for all samples with increasing nonconvexity η .

isotropic compaction, q/p is nearly zero in the initial state ($\varepsilon_q = 0$). Then, as we assume that the particles are perfectly rigid and because of the high packing fraction, the shear strength jumps to a peak stress before relaxing to a constant plateau named “residual” state. We see that the value q/p at the peak and residual states increases with η . The normalized residual stress $(q/p)^*$ is independent of the initial state, and it represents the intrinsic shear strength of the material corresponding to the internal angle of friction φ^* given in 3D by:

$$\sin \varphi^* = \frac{3(q/p)^*}{2 + (q/p)^*}. \quad (12)$$

Figure 4 shows the variation of $(q/p)^*$ and $\sin \varphi^*$ averaged in the residual state as a function of η . The error bars represent the standard deviation computed from the fluctuations around the mean in the residual state in the interval $\varepsilon_q \in [0.5, 0.9]$ as observed in Fig. 3. We see that $(q/p)^*$ and $\sin \varphi^*$ increase with η at decreasing rate. This increase of shear strength reflects the effect of interlocking due to particle nonconvexity as we shall see in section IV. In a recent work, the quasi-static rheology of granular packings of elongated [25, 27], angular [26] and non-convex particles [36, 37] in 2D where systematically analyzed by means of the parameter η . A similar ascending trend of shear strength with a trend to saturation was found as a function of η , showing that this low-order parameter is a generic shape parameter, underlying to a large extent the effect of particle shape.

C. Packing fraction

In Fig. 5, the evolution of packing fraction ρ is shown as a function of ε_q for all values of η . All samples dilate during shear and ρ declines from its value ρ^0 in the initial isotropic state down to a constant value ρ^* in the residual state. The samples dilate almost homogeneously at low shear strains (≤ 0.3) and thus ρ decreases rapidly. At larger strains, dilation is localized within shear bands

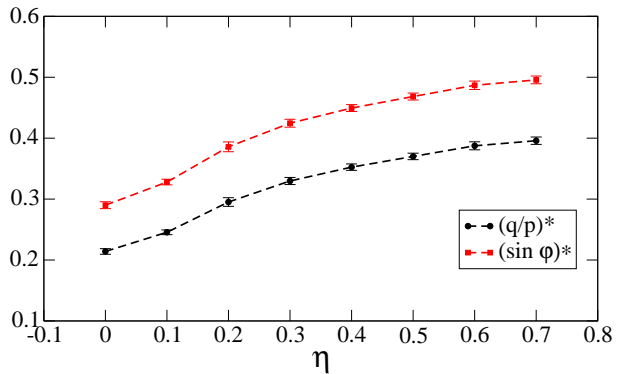


FIG. 4: (Color Online) Normalized shear stress $(q/p)^*$ (black circle) and friction angle $(\sin \varphi)^*$ (red square) averaged in the residual state as a function of non-convexity parameter η .

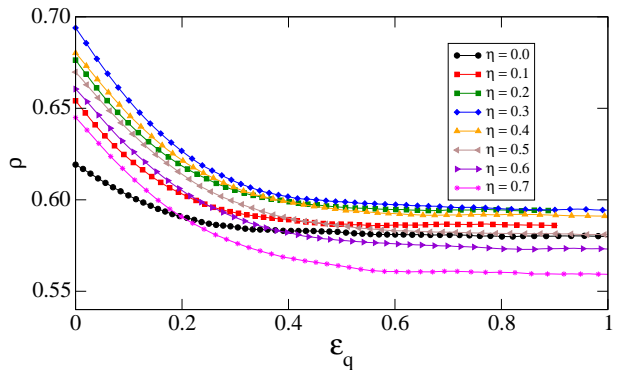


FIG. 5: (Color Online) Evolution of packing fraction ρ with the cumulative shear strain ε_q for different values of η .

appearing throughout the system. Figure 6 shows a grey level map of particle velocities in a portion of packing for $\eta = 0.6$ at $\varepsilon_q = 0.65$ revealing the shear band in the material. As the shear bands develop inside the system, different locations of the sample dilate at different times, and a nearly homogeneous density ρ^* is reached only at $\varepsilon_q = 0.5$. For our rigid particles the residual packing fraction ρ^* is independent of the confining pressure and it should be considered as an intrinsic property of the material, i.e. reflecting basically the particle shape and size distribution as well as the friction coefficient between particles.

Figure 7 displays ρ_0 and ρ^* as a function of η . Remarkably, in both cases, the packing fraction first grows from its value for spheres ($\eta = 0$) towards a maximum at $\eta = 0.3$ and then declines at higher values of η . The peak value of packing fraction ρ_0 in the isotropic state is as high as 0.70. In the residual state, the packing fraction ρ^* takes as values as low as 0.55 at $\eta = 0.7$. This unmonotonic variation of the packing fraction as a function of nonconvexity shows the complexity of granular textures created by nonspherical particles. On intuitive grounds, it might be expected that by increasing nonconvexity, the packing fraction would increase as a result of

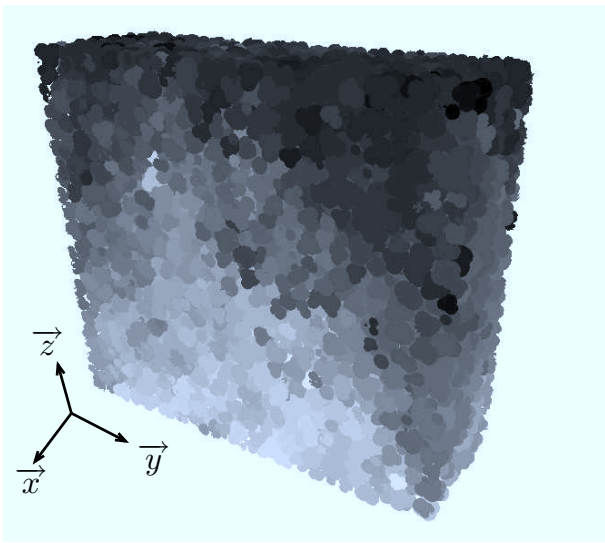


FIG. 6: Grey level map of particle velocities in a portion of the packing at $\varepsilon_q \simeq 0.65$ for $\eta = 0.6$.

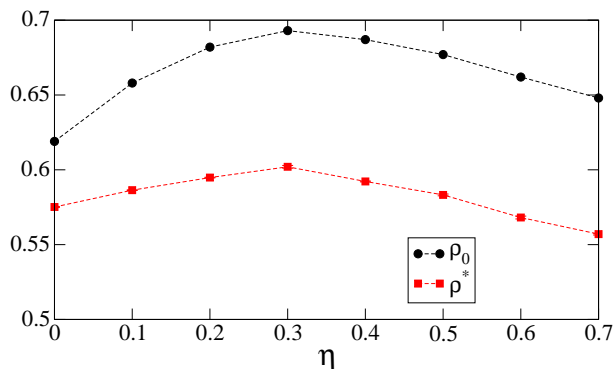


FIG. 7: (Color Online) Packing fraction ρ as a function of η both in the initial isotropic state (black) and in the residual state (red).

reinforced interlocking between particles. This is clearly not the prevailing mechanism in the range $\eta > 0.3$.

A similar unmonotonic behavior of the packing fraction was previously observed for granular packings composed of nonconvex particles in 2D [36–38], as well as for elongated particles such as ellipses, ellipsoidal particles, spherocylinders and rounded-cap rectangles [4, 25, 29–31]. For elongated particles, the fall-off of the packing fraction at higher aspect ratios is attributed to the increase of the largest pore volume that can not be filled by a particle. A similar effect can be advocated for our nonconvex particles which can form an increasingly tortuous and large pore space as the nonconvexity increases.

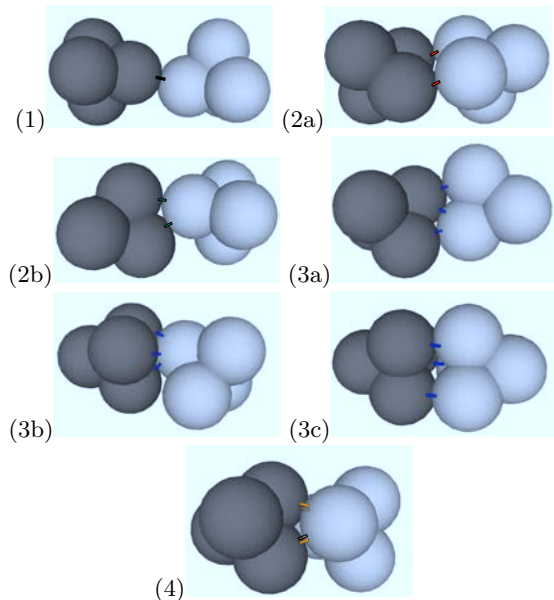


FIG. 8: (Color Online) Contacts configurations between two particles : (1) “simple” contacts named (s), (2a) “double-simple” contacts (ds), (2b) “double” contacts (d), (3a, 3b, 3c) “triple” contacts (t) and (4) “quadruple” (q) contacts.

IV. GRANULAR TEXTURE

A. Contact/neighbors network topology

In this section, we investigate the general organization (texture) of our packings in terms of particle connectivity. The main effect of shape nonconvexity is to allow for multiple contacts between aggregates as shown in Fig. 8. Seven different types of contacts can occur between two particles: 1) “simple” contacts (s), 2) “double-simple” contacts (ds) defined as two simple contacts between two pairs of spheres, 3) “double contacts” (d) defined as two contacts between one sphere of one aggregate and two spheres belonging on the other aggregate, 4) “triple” contacts (t) defined as a combination of simple and double contacts or one sphere of one aggregate and three spheres of another aggregate or three simple contacts, 5) “quadruple” contacts (q) defined as a combination of two double contacts, and 6) five or six contacts with a negligible proportion (below 1%) compared to other contact types.

Thus, given multiple contacts between aggregates, we can distinguish between the coordination number Z as the mean number of neighbors per particle (multiple contacts seen as one contact), and the “connectivity” number Z_c defined as the mean number of contacts per particle. For spherical particles we have $Z = Z_c$. Considering only the contact types s , ds , t and q and neglecting higher-order contacts, we get

$$\frac{Z_c}{Z} = k_s + 2(k_{ds} + k_d) + 3k_t + 4k_q \quad (13)$$

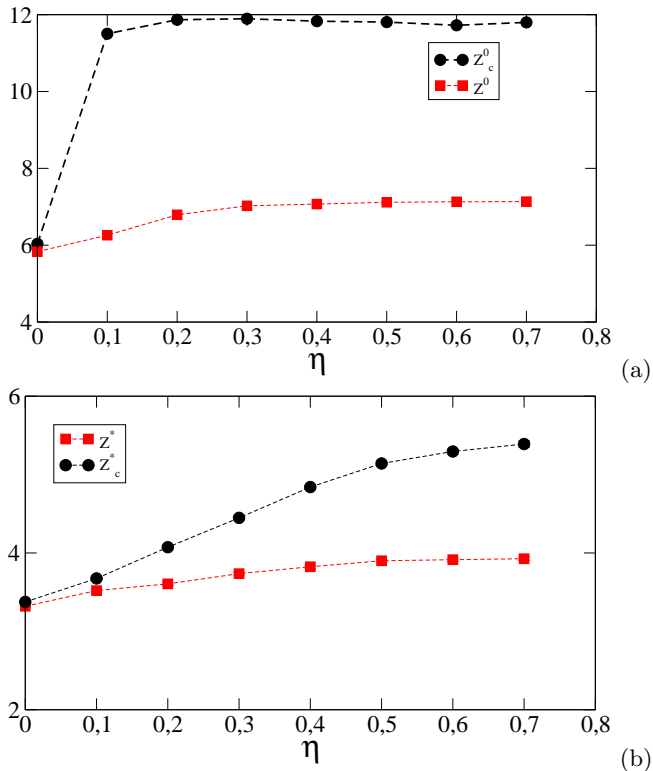


FIG. 9: (Color Online) Coordination Z and connectivity Z_c numbers as a function of η in both initial (a) and residual (b) states.

where k_s , k_{ds} , k_d , k_t and k_q are the proportions of s , ds , d , t and q contacts. Figure 9 displays Z and Z_c in the isotropic and residual states as a function of η . The exponents 0 and * refer to the isotropic and residual states, respectively. We see that Z_c^0 jumps from 6 for spheres to $\simeq 12$ for $\eta > 0$. This jump is compatible with the isostatic nature of our packings prepared with a zero friction coefficient [55]. Frictionless spheres are characterized by three degree of freedom (rotations being immaterial) so that the isostatic condition implies three independent constraints (normal forces) which amounts to a connectivity number of 6. For non-spherical particles, the particle rotations become material and a similar counting argument leads to a connectivity number of 12. For frictional aggregates, in the residual state, Z_c^* is lower but increases from 3.5 to 5.5 with η . Interestingly, we also see that, in both isostatic and residual states, Z increases much less slowly with η than Z_c . In others words, as in 2D case [36, 37], the effect of increasing nonconvexity is expressed by an increasing number of multiple contacts with the same average number of neighboring aggregates and therefore at large values of η the packings are loose but well connected.

To get further insight into the connectivity of the contact network, we plot in Fig.10 the proportion of each contact type in the isotropic and residual states as a function of η . We observe that the proportion of different types of connection between aggregates are nearly inde-

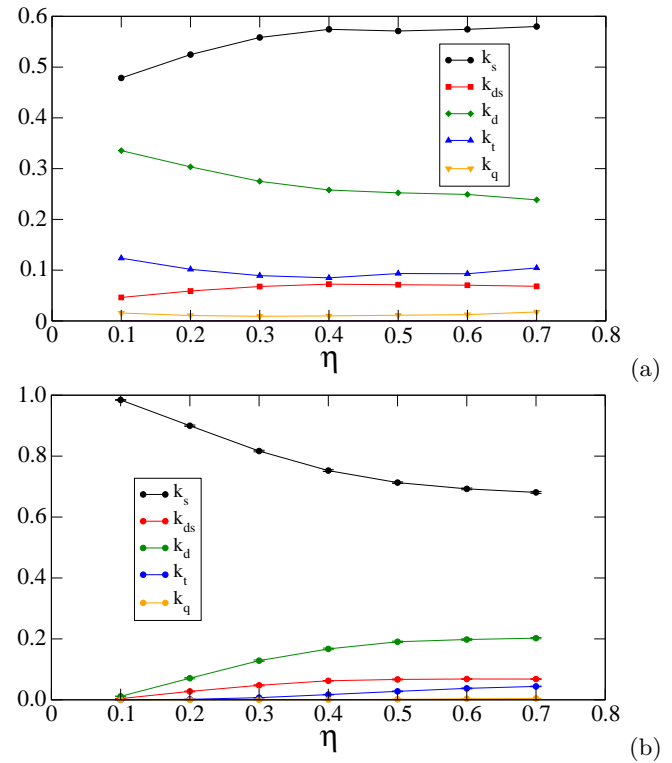


FIG. 10: (Color Online) Proportions of simple, double, double-simple, triple and quadruple contacts as a function of η in the isotropic (a) and residual (b) states.

pendent of η in the isostatic state. The simple contacts represent the highest proportion ($\simeq 0.56$) whereas ds , t and q contacts have the lowest proportions (≤ 0.15). The d contacts are represented by an intermediate proportion of nearly 0.3. In the residual state, the proportion of simple contacts declines as η is increased but its value remains above that in the isotropic state at the expense of the increasing number of other contact types, which are less in number.

We observe also a drastic loss of double contacts in the residual state compared to the initial isotropic state for all values of η , whereas the proportion of double-simple and triple contacts are nearly the same and the proportion of quadruple contacts is nearly zero. This can be explained by the fact that residual state is governed by shear-induced dilation. In this, the particles explore constantly metastable states and thus double, multiple contacts are less involved in the stability of the packing. In contrast, the isostatic state corresponds to the unique minimum of the total potential energy $\sigma_0 V$ of the packing. This state is achieved by enhanced number of double and triple contacts which by interlocking contribute to increase the packing fraction.

The description of the microstructure in terms of the average coordination and connectivity between the aggregates provides a clear picture of the effect of shape non-convexity. It is also remarkable that the trends observed here by 3D simulations are nearly identical to those ob-

served by Saint-Cyr et al. and Szarf et al. by means of 2D simulations [36, 37]. In the following, we analyze higher-order descriptors of the microstructure and their relationship to the macroscopic behaviour.

B. Fabric and branch-length anisotropy

A well known feature of dry granular materials is that the shear strength is related to the buildup of an anisotropic structure during shear due to 1) friction between the particles and 2) as a result of steric effects depending on particle shape [56]. A common approach used by various authors is to consider the probability distribution $P(\mathbf{n})$, where \mathbf{n} is the unit vector of contact normals in the *contact frame* (\mathbf{n}, \mathbf{t}) where \mathbf{t} is an orthonormal unit vector oriented along the tangential force as illustrated in Fig. 11(a). In 3D, let $\Omega = (\theta, \phi)$ be the angles that define the orientation of \mathbf{n} where θ is the radial angle and ϕ the azimuthal angle as defined in Fig.11(c). From numerical data we can then evaluate the probability density functions $P_\Omega(\Omega)$ of contacts pointing along a direction Ω .

We have seen previously that, due to multiple contacts between nonconvex particles, the contact network is different from the network of neighboring particles. Thus, in addition to the distribution $P(\mathbf{n})$ of contact normals \mathbf{n} , we define the probability distribution $P(\mathbf{n}')$ for the neighbor network, where \mathbf{n}' is the unit *branch vector* joining the centers of two touching aggregates and pointing in a direction $\Omega' = (\theta', \phi')$. We also associate a local frame $(\mathbf{n}', \mathbf{t}')$ with \mathbf{t}' an orthonormal unit vector; see Fig.11(b). Under the axisymmetric conditions of our simulations, P_Ω and $P_{\Omega'}$ are independent of the azimuthal angle ϕ and ϕ' so that we may consider in the following only the probability densities P_θ and $P_{\theta'}$ of the radial angles θ and θ' .

The inset to figure 12 displays a polar representation of the above functions in the θ -plane in the critical state for $\eta = 0.4$. We observe an anisotropic behavior in all cases. The peak value occurs along the compressive axis ($\theta_c = \theta'_c = \pi/2$) and coincides with the principal stress direction $\theta_\sigma = \pi/2$. The peak is less marked for $P_{\theta'}$ than for P_θ . The simple shapes of the above functions suggest that harmonic approximation based on spherical harmonics at leading terms captures the anisotropies of both neighbor and contact networks. There are nine second-order basis functions $Y_m^l(\Theta, \Phi)$ [11, 28], where (Θ, Φ) stands either for (θ, ϕ) or for (θ', ϕ') depending on the local frame used, but only the functions compatible with the symmetries of the problem (i.e. independent with respect to Φ and π -periodic with Θ) are admissible. The only admissible functions are therefore $Y_0^0 = 1$ and $Y_2^0 = 3 \cos^2 \Theta - 1$. Hence, within a harmonic model of fabric, we have:

$$P_\Theta(\Theta) = \frac{1}{4\pi} \{1 + \bar{a}_c [3 \cos^2(\Theta - \Theta_c) - 1]\}, \quad (14)$$

where $(\bar{a}_c, \Theta_c) = (a_c, \theta_c)$ are the contact anisotropy and the privileged contact direction of the contact network

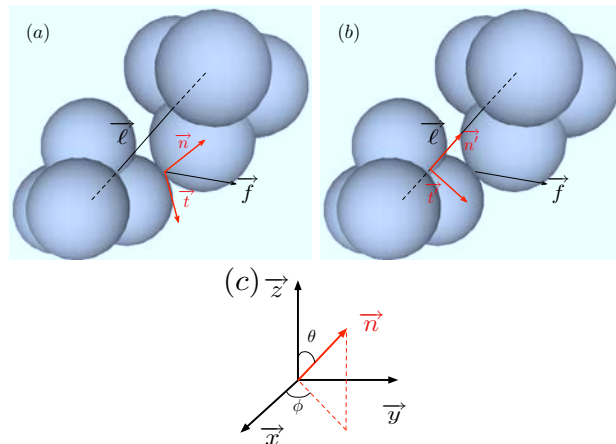


FIG. 11: (Color Online) (a) Contact frame (\mathbf{n}, \mathbf{t}) , (b) Inter-center frame $(\mathbf{n}', \mathbf{t}')$, (c) Azimuthal angle Φ and radial angle Θ .

and $(\bar{a}_c, \Theta_c) = (a'_c, \theta'_c)$ are branch anisotropy and the privileged branch direction of the neighbor network. In practice, the values of \bar{a}_c can be calculated from generalized fabric tensors as described in [28].

Figure 12 shows the variation of a_c and a'_c averaged in the residual state as a function of η . We see that both anisotropies increases with η from 0.2 to a nearly constant value of 0.3 and 0.36, respectively, beyond $\eta > 0.4$. We also have $a'_c < a_c$. The saturation of a'_c in the residual state is compatible with the saturation of Z , which represents the coordination number of the network of neighbors, as observed in Fig. 9. On the other hand, a_c slightly increases as Z_c with η due to enhanced interlocking and gain of contacts with the same neighboring aggregates (since Z is nearly independent of η in the range $\eta > 0.4$). Hence, the effect of the nonconvexity of the aggregates on the texture manifests itself by increasing coordination, connectivity and contact anisotropy in the range $\eta \leq 0.4$ and by enhanced connectivity and anisotropy due to interlocking.

This increase of interlocking can be also observed for the projections $l_n \mathbf{n}$ and $l_t \mathbf{t}$ of the branch vector $l_{n'} \mathbf{n}'$ along the normal and tangential forces, respectively. In close correlation with contact and branch anisotropies, we can define the average angular dependance of this quantity. We consider the joint probability density $P(l_n, \mathbf{n})$, $P(l_t, \mathbf{t})$ and $P(l_{n'}, \mathbf{n}')$ of the normal, tangential and radial branch lengths. We have the three following expressions:

$$\langle l_n \rangle(\Omega) P_\Omega(\Omega) = \int_0^\infty l_n P(l_n, \mathbf{n}) dl_n, \quad (15)$$

$$\langle l_t \rangle(\Omega) P_\Omega(\Omega) = \int_0^\infty l_t P(l_t, \mathbf{t}) dl_t, \quad (16)$$

$$\langle l_{n'} \rangle(\Omega') P_{\Omega'}(\Omega') = \int_0^\infty l_{n'} P(l_{n'}, \mathbf{n}') dl_{n'}, \quad (17)$$

where $\langle l_n \rangle(\Omega)$, $\langle l_t \rangle(\Omega)$ and $\langle l_{n'} \rangle(\Omega')$ are the average nor-

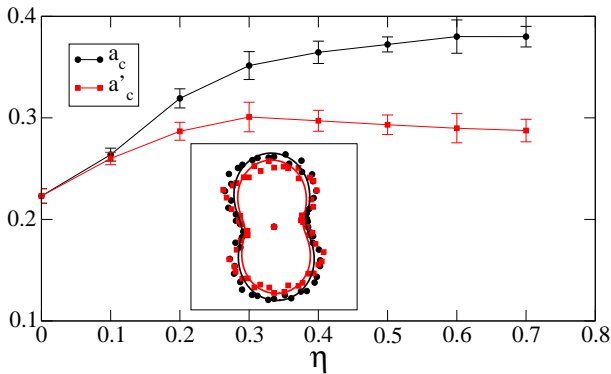


FIG. 12: (Color online) Contact anisotropy a_c (black circles) and branch vector anisotropy a'_c (red/gray squares) as a function of shape parameter η averaged in residual state. The error bars represent the standard deviation in the residual state. The inset shows the angular probability densities $P_\theta(\theta)$ in black circle and $P_{\theta'}(\theta')$ in red/gray squares for $\eta = 0.4$ calculated from the simulations (data points) together with the harmonic approximation (lines).

mal, tangential and radial lengths along the directions Ω and Ω' , respectively [28]. The mean normal, tangential and radial lengths are simply given by:

$$\langle \ell_n \rangle = \frac{1}{4\pi} \int_{\mathcal{S}} \langle \ell_n \rangle(\Omega) P_\Omega(\Omega) d\Omega, \quad (18)$$

$$\langle \ell_t \rangle = \frac{1}{4\pi} \int_{\mathcal{S}} \langle \ell_t \rangle(\Omega) P_\Omega(\Omega) d\Omega, \quad (19)$$

$$\langle \ell_{n'} \rangle = \frac{1}{4\pi} \int_{\mathcal{S}} \langle \ell_{n'} \rangle(\Omega') P_{\Omega'}(\Omega') d\Omega', \quad (20)$$

where \mathcal{S} is the integration domain $[0, \pi] \times [0, 2\pi]$. $\langle \ell_n \rangle$ and $\langle \ell_{n'} \rangle$ are always positive by construction. In contrast ℓ_t can be negative and we get $\langle \ell_t \rangle \sim 0$ in all our simulations. This condition implies that the functions $\langle \ell_t \rangle(\Omega)$ and $P_\Omega(\Omega)$ are orthonormal. Moreover, under the axisymmetric conditions of our simulations, these functions are independent of the azimuthal angles ϕ and ϕ' . These functions can then be expanded at first order over a spherical harmonic basis as follows:

$$\langle \ell_{\bar{n}} \rangle(\Theta) = \langle \ell_{\bar{n}} \rangle \{1 + a_{l_{\bar{n}}} [3 \cos^2(\Theta - \Theta_{l_{\bar{n}}}) - 1]\}, \quad (21)$$

$$\langle \ell_t \rangle(\theta) = \langle \ell_n \rangle a_{l_t} \sin 2(\theta - \theta_{l_t}), \quad (22)$$

where $(\ell_{\bar{n}}, a_{l_{\bar{n}}}, \Theta_{l_{\bar{n}}}) = (\ell_n, a_{l_n}, \theta_{l_n})$ are the normal branch-length anisotropy and privileged orientation of $\langle \ell_n \rangle(\theta)$ in the frame (\mathbf{n}, \mathbf{t}) , $(\ell_{\bar{n}'}, a_{l_{\bar{n}'}}), \Theta_{l_{\bar{n}'}} = (\ell_{n'}, a_{l_{n'}}, \theta_{l_{n'}})$ are the radial branch-length anisotropy and privileged orientation of $\langle \ell_{n'} \rangle(\theta')$ in $(\mathbf{n}', \mathbf{t}')$, and (a_{l_t}, θ_{l_t}) are the tangential branch-length anisotropy and the privileged orientation of $\langle \ell_t \rangle(\theta)$ in (\mathbf{n}, \mathbf{t}) , respectively.

The inset to Figure 13 shows the polar diagrams of the simulation data for $\langle \ell_n \rangle(\theta)$, $\langle \ell_t \rangle(\theta)$ and $\langle \ell_{n'} \rangle(\theta')$ at $\eta = 0.4$, together with the harmonic approximations in the residual state. We see that the distribution of normal and radial branch length are nearly isotropic, whereas

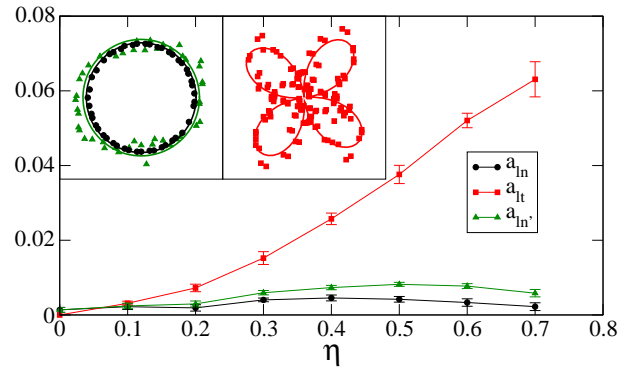


FIG. 13: (Color online) Normal and tangential branch length anisotropies a_{l_n} (circles) and a_{l_t} (squares), and branch-length anisotropy $a_{l_{n'}}$ (triangles) as a function of shape parameter η in the residual state. The error bars represent the standard deviation in the residual state. The inset shows the angular average functions $\langle \ell_{l_n} \rangle(\theta)$, $\langle \ell_{l_t} \rangle(\theta)$ and $\langle \ell_{l_{n'}} \rangle(\theta)$ in black (circle), red (dark gray square) and green (light gray triangle), respectively, for $\eta = 0.4$, calculated from the simulation data (points) and approximated by harmonic fits (lines).

the distribution of tangential branch-length components has two modes along the directions $\theta_t \pm \pi/4$. The variation of normal, tangential and radial length anisotropies are plotted in Fig. 13 as a function of η . We see that $a_{l_n} \sim a_{l_{n'}} \sim 0$. This is due to the absence of shape eccentricity of the particles [25, 27, 28, 35, 57, 58] and also because of the low span in the particle size distribution [46]. This shows that, even if the particles and contacts are nonuniformly distributed around each particle, the mean distance between particles remaining nearly constant. In contrast, we see that a_{l_t} increases with η from 0 to 0.06. These values are weak but their global increase is directly related to the increase of interlocking. In fact, the tangential projection of the branch vector ℓ_t on the contact plane between two aggregates increases with interlocking. This leads to the increase of the ratio ℓ_t/ℓ_n for the interlocked aggregates and thus the average value $\langle \ell_t \rangle/\langle \ell_n \rangle$ at $\theta = \theta_{l_t} + \pi/4$, that is equal to a_{l_t} according to equation (22).

V. FORCE TRANSMISSION

A. Force distribution

We consider in this section the distribution of contact forces, which reflects the inhomogeneity of the contact network [47, 59–61]. The normal force pdf's averaged in the residual state are shown in Fig. 14 in log-linear (a) and log-log (b) scale for all values of η . The distribution becomes increasingly broader as the nonconvexity increases but the relative changes are surprisingly small. Indeed, the maximum force varies from ten times the mean force for spheres to twelve times the mean force for $\eta = 0.7$. We observe also an increasing number of contacts carry-

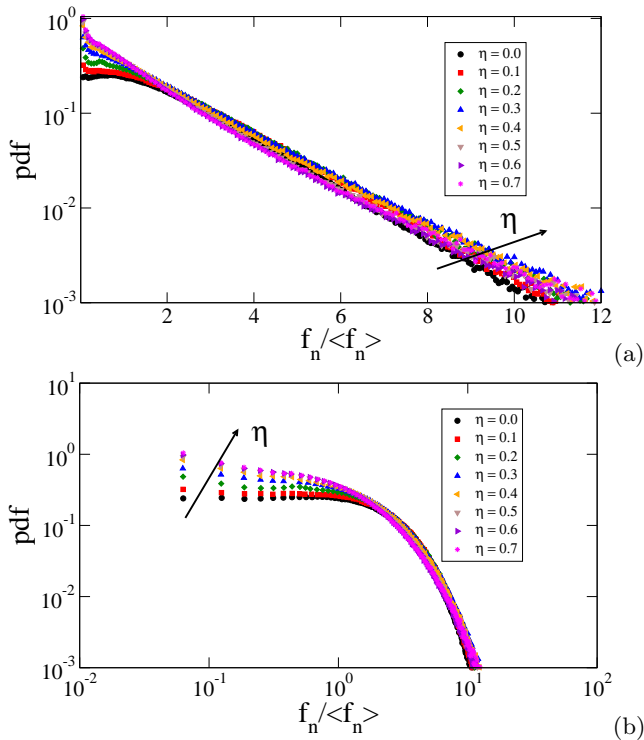


FIG. 14: (Color online) Probability density functions of normal forces in log-linear (a) and log-log scales (b).

ing weak forces (below the mean) as η increases. This rather small change of the distributions with η may be attributed to the fact that the contacts are always between the spheres belonging to the aggregates and from this viewpoint the distribution of forces is not very different from that for a packing of spheres.

Another way to highlight the role of multiple contacts in force transmission is to consider the reaction forces between aggregates. The reaction force \mathbf{F} between two aggregates is the resultant of point forces acting at their contacts, and it can be projected on the intercenter-frame. In this way, the contact-force network can be replaced by the simplest *neighbor-force* network carrying the radial forces $f_{n'} = \mathbf{F}\mathbf{n}'$. Figure 15(a) shows the neighbor-force network in the residual state for $\eta = 0.6$. The “force forest” observed in this figure represents the force chains along the branch vectors. Figure 15(b) shows the same snapshot where the radial forces are colored according to the contact type. It seems that stronger force chains are composed essentially of double and double-simple contacts and occasionally mediated by simple, triple and quadruple contacts.

The radial force pdf’s averaged in the residual state are shown in Fig.16 in log-linear (a) and log-log (b) scale for all values of η . The distribution becomes broader than contact force distributions as nonconvexity is increased. We observe both an increasing number of weak forces and stronger forces. This means that the packings of more nonconvex aggregates, though more closely connected,

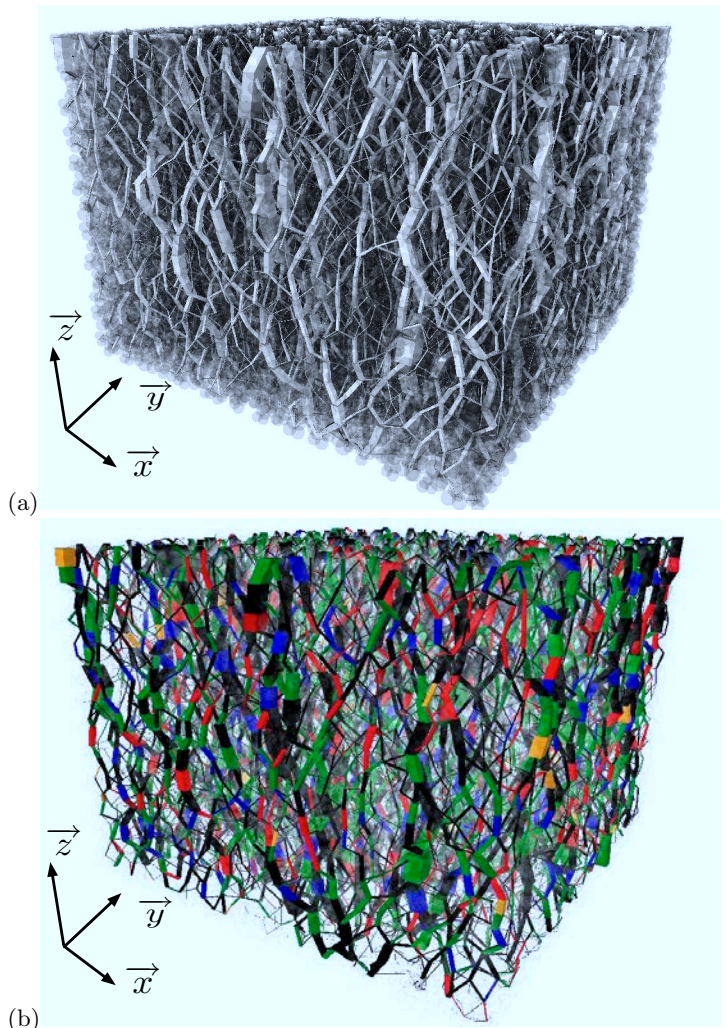


FIG. 15: (Color online) Snapshot of radial forces for $\eta = 0.6$. Line thickness is proportional to the radial force (a). In (b) the forces are plotted in different colors depending on contact types: *s*-contacts in black, *d*-contacts in red, *ds*-contacts in green, *t*-contacts in purple and *q*-contacts in yellow.

are more inhomogeneous in terms of radial forces.

The anisotropic structures seen in Fig.15 can be characterized more generally through the angular dependence of the average normal and radial forces via the same methodology as that given in section IV for branch-length orientations. Considering the joint probability densities $P(f_n, \mathbf{n})$ and $P(f_{n'}, \mathbf{n}')$ of the normal and radial forces, we have:

$$\langle f_{\bar{n}} \rangle(\bar{\Omega}) P_{\bar{\Omega}}(\bar{\Omega}) = \int_0^\infty f_{\bar{n}} P(f_{\bar{n}}, \bar{\Omega}) df_{\bar{n}}, \quad (23)$$

where (\bar{n}, Θ) stands alternatively for (n, θ) in the contact frame or for (n', θ') in the branch frame. $\langle f_n \rangle(\Omega)$ and $\langle f_{n'} \rangle(\Omega')$ are the average normal and radial forces along the directions θ and θ' , respectively. The average

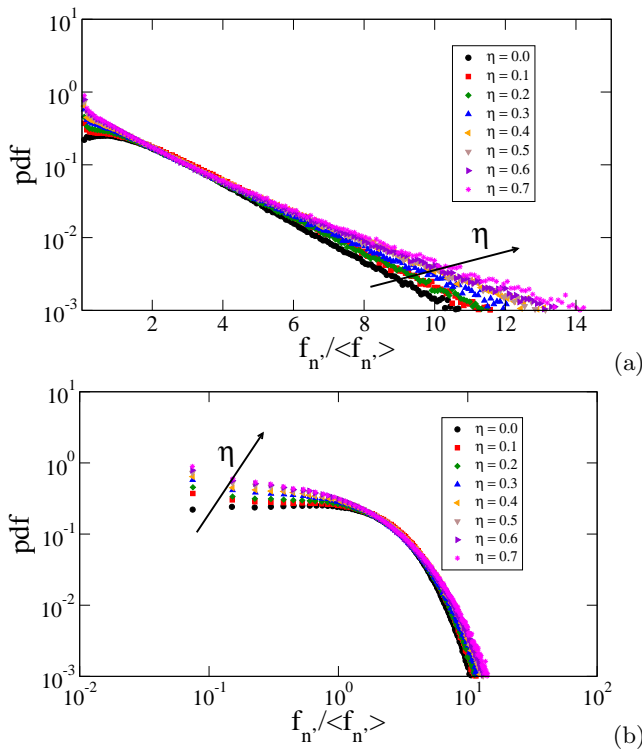


FIG. 16: (Color online) Probability density functions of radial forces in log-linear (a) and log-log scales (b).

normal/radial force is given by:

$$\langle f_{\bar{n}} \rangle = \frac{1}{4\pi} \int_{\mathcal{S}} \langle f_{\bar{n}} \rangle(\bar{\Omega}) P_{\bar{\Omega}}(\bar{\Omega}) d\bar{\Omega}, \quad (24)$$

Under the axisymmetric conditions of our simulations, the above probability density functions are independent of the azimuthal angle ϕ and can be expanded on a spherical harmonics basis as follows:

$$\langle f_{\bar{n}} \rangle(\Theta) = \langle f_{\bar{n}} \rangle \{1 + a_{\bar{n}} [3 \cos^2(\Theta - \Theta_{\bar{n}}) - 1]\}, \quad (25)$$

where, $(f_{\bar{n}}, a_{\bar{n}}, \Theta_{\bar{n}}) = (f_n, a_n, \theta_n)$ are the normal force anisotropy and privileged orientation of $\langle f_n \rangle(\theta)$ in (\mathbf{n}, \mathbf{t}) , and $(f_{\bar{n}}, a_{\bar{n}}, \Theta_{\bar{n}}) = (f_{n'}, a_{n'}, \theta_{n'})$ are the radial force anisotropy and privileged orientation of $\langle f_{n'} \rangle(\theta')$ in $(\mathbf{n}', \mathbf{t}')$. This form is well fit to the data as shown in the inset of Fig. 17 in the residual state for $\eta = 0.4$. We also see that both θ_n and $\theta_{n'}$ coincide with the principal stress direction $\theta_{\sigma} = \pi/2$.

The residual-state value of a_n and $a_{n'}$ are displayed together in Fig. 17 as a function of η . We see that $a_{n'} > a_n$ and that both anisotropies increase with η from 0.2 to 0.33 for a_n and to 0.43 for $a_{n'}$. The large variation of $a_{n'}$ with η is consistent with the fact that the pdf of radial forces is increasingly broader with η . Moreover, the increase of a_n and $a_{n'}$ in connection to the saturation of a_c and a'_c (see section IV) implies that stronger force chains are transmitted through the principal stress direction while in average the mean orientation of contacts

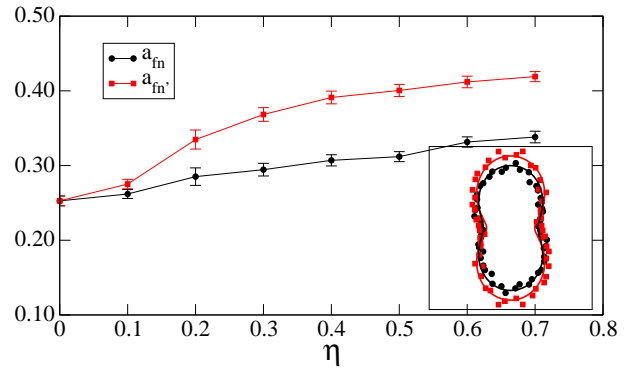


FIG. 17: (Color online) Normal and radial force anisotropies a_n (black circle) and $a_{n'}$ (red squares) as a function of η in the residual state. The error bars represent the standard deviation in the residual state. The inset shows the angular average functions $\langle f_n \rangle(\theta)$ and $\langle f_{n'} \rangle(\theta)$ in black and red, respectively, for $\eta = 0.4$ calculated from the simulation data (points) together with the harmonic approximation (lines). The error bars represent the standard deviation in the residual state.

remains unchanged at larger η . This can be attributed to the increase of the proportion of multiple contacts between particles. Indeed, by restricting the summation in equation (4) to each contact type, one may partition the stress tensor as a sum of partial stress tensors:

$$\boldsymbol{\sigma} = \boldsymbol{\sigma}_s + \boldsymbol{\sigma}_{ds} + \boldsymbol{\sigma}_d + \boldsymbol{\sigma}_t + \boldsymbol{\sigma}_q, \quad (26)$$

where $\boldsymbol{\sigma}_s$, $\boldsymbol{\sigma}_{ds}$, $\boldsymbol{\sigma}_d$, $\boldsymbol{\sigma}_t$ and $\boldsymbol{\sigma}_q$ represent the stresses carried by different contact types. The corresponding stress deviators q_s , q_{ds} , q_d , q_t and q_q averaged in the residual state and normalized by the mean stress p are shown in Fig.18 as a function of η . It is remarkable that the shear stress q_s/p supported by simple contacts remains nearly independent of η and equal to ~ 0.2 whereas the proportion of simple contacts decreases drastically with η from 1 to 0.65 as it was seen in section IV. Hence, the increase of shear strength with η is mainly due to the increase of q_d/p and to a lesser extent to the other contacts. In this way, the growth of the number of interlocked contacts is clearly at the origin of enhanced shear strength of the packings as η increases.

B. Friction mobilization

The mobilization of friction forces is a basic parameter in granular materials. A simple way to quantify the friction mobilization in granular materials is to consider the proportion S of sliding contacts, i.e. the contacts where the friction force f_t equals μf_n in absolute value in steady shearing. Figure 19 displays S in the residual state as a function of η . We see that S increases from 0.23 for spheres to 0.7 for $\eta = 0.7$. Another key information is that the sliding contacts are unevenly distributed among simple, double-simple, double, triple and quadruple contacts, as shown in Fig. 20. Only a weak num-

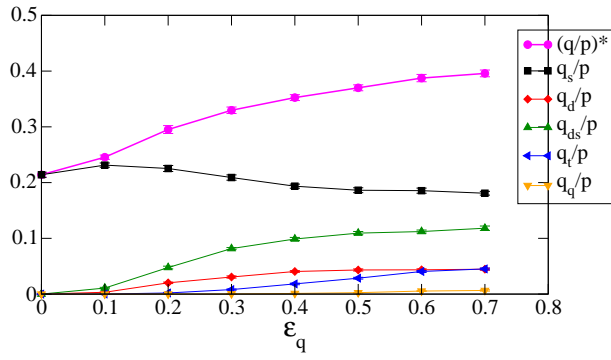


FIG. 18: (Color online) Normalized shear stress supported by s , ds , t and q contact as a function of η .

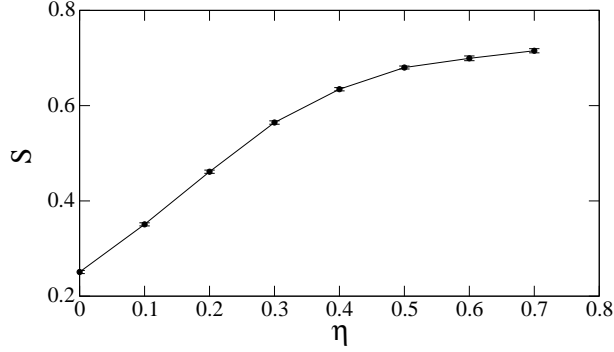


FIG. 19: (Color online) Proportion of sliding contacts as a function of η in the residual state. Error bars show the standard deviation in the residual state.

ber of double-simple, triple and quadruple contacts are sliding whereas the proportion of sliding double contacts increases with η at the expense of simple contacts.

A somewhat more elegant way of describing friction mobilization is to consider the proportion of contacts in correlation with the friction force. We consider the probability density of the tangential and orthoradial forces $f_t \mathbf{t} = f_n \mathbf{n}' - \mathbf{f}$ and $f_{t'} \mathbf{t}' = f_n \mathbf{n}' - \mathbf{f}$, respectively, which derive from the joint probability densities $P(f_t, \mathbf{t})$ and

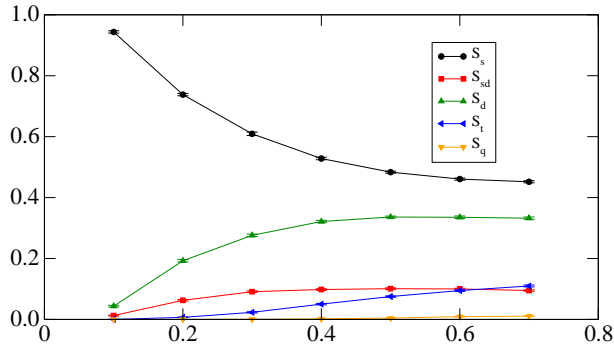


FIG. 20: (Color online) Proportion of sliding contacts as a function of η in the residual state for different contact types. Error bars show the standard deviation in the residual state.

$P(f_{t'}, \mathbf{t}')$, of the tangential f_t and orthoradial $f_{t'}$ forces along the directions \mathbf{t} and \mathbf{t}' , respectively. Thus, as for normal and radial forces, we have:

$$\langle f_{\bar{t}} \rangle(\bar{\Omega}) P_{\bar{\Omega}}(\bar{\Omega}) = \int_0^\infty f_{\bar{t}} P(f_{\bar{t}}, \bar{\Omega}) df_{\bar{\Omega}}, \quad (27)$$

where (\bar{t}, Θ) stands alternatively for (t, θ) in the contact frame or for (t', θ') in the branch frame. $\langle f_t \rangle(\Omega)$ and $\langle f_{t'} \rangle(\Omega')$ are the average tangential and orthoradial force along the directions θ and θ' , respectively. The average tangential/orthoradial radial force is given by:

$$\langle f_{\bar{t}} \rangle = \frac{1}{4\pi} \int_{\bar{\Omega}} \langle f_{\bar{t}} \rangle(\bar{\Omega}) P_{\bar{\Omega}}(\bar{\Omega}) d\bar{\Omega}. \quad (28)$$

Remarking now that, in quasistatic deformation the force accelerations are negligible so that the forces and force moments acting on the aggregate a are balanced, we have:

$$\sum_{c \in a} \mathbf{f}^c = 0, \quad (29)$$

$$\sum_{c \in a} \{r_n^c f_t^c + r_t^c f_n^c\} = 0, \quad (30)$$

where $r_n^c = \mathbf{r}^c \cdot \mathbf{n}$ and $r_t^c = \mathbf{r}^c \cdot \mathbf{t}$, where \mathbf{r}^c is the *contact vector* joining the center of inertia of the aggregate a to the contact c . Taking the average of equation 30 over all aggregates a , and assuming that ℓ_n , f_t and ℓ_t , f_n are statistically independent, we get $\langle \ell_n \rangle \langle f_t \rangle = \langle \ell_t \rangle \langle f_n \rangle$. As mentioned in section IV, $\langle \ell_t \rangle = 0$, thus as $\langle \ell_n \rangle > 0$, the average tangential force in the packing vanishes. Similarly, considering the contacts projected on the branch frame $(\mathbf{n}'^c, \mathbf{t}'^c)$, we have $\langle f_{t'} \rangle = 0$.

Since the average tangential and orthoradial forces vanish, $\langle f_{\bar{t}} \rangle(\bar{\Omega})$ and $P_{\bar{\Omega}}(\bar{\Omega})$ are orthonormal. Given that under the axisymmetric conditions of our simulations these probability density functions are independent of the azimuthal angle ϕ , these functions can thus be expanded over a spherical harmonics basis as follows:

$$\langle f_t \rangle(\theta) = \langle f_n \rangle a_{ft} \sin 2(\theta - \theta_t), \quad (31)$$

$$\langle f_{t'} \rangle(\theta') = \langle f_{n'} \rangle a_{f_{t'}} \sin 2(\theta - \theta_{t'}), \quad (32)$$

where, (a_t, θ_t) are the tangential anisotropy and privileged orientation of $\langle f_t \rangle(\theta)$ in the frame (\mathbf{n}, \mathbf{t}) , and $(a_{t'}, \theta_{t'})$ are the orthoradial anisotropy and privileged orientation of $\langle f_{t'} \rangle(\theta')$ in the frame $(\mathbf{n}', \mathbf{t}')$.

The inset of Figure 22 shows polar diagrams of the simulation data for $\langle f_t \rangle(\theta)$ and $\langle f_{t'} \rangle(\theta')$ together with plots of the function (31) in the residual state for $\eta = 0.4$. We see that the function fits excellently the data. We also see that $\theta_t = \theta_{t'} = \pi/2$ coincides with the principal stress direction. We thus define a friction mobilization function [28, 35]:

$$\bar{M}_{fric}(\Theta) = \frac{\langle f_{\bar{t}} \rangle(\Theta)}{\bar{\mu} \langle f_{\bar{n}} \rangle} = \frac{a_{\bar{t}}}{\bar{\mu}} \sin 2(\Theta - \Theta_{\bar{t}}), \quad (33)$$

where $\bar{\mu} = \mu$ and $(a_{\bar{t}}, \Theta_{\bar{t}}) = (a_t, \theta)$ in the local contact frame and $\bar{\mu} = \langle (f_{n'}/f_n) \sqrt{(1 + \mu^2) - (f_n/f_{n'})^2} \rangle$ and

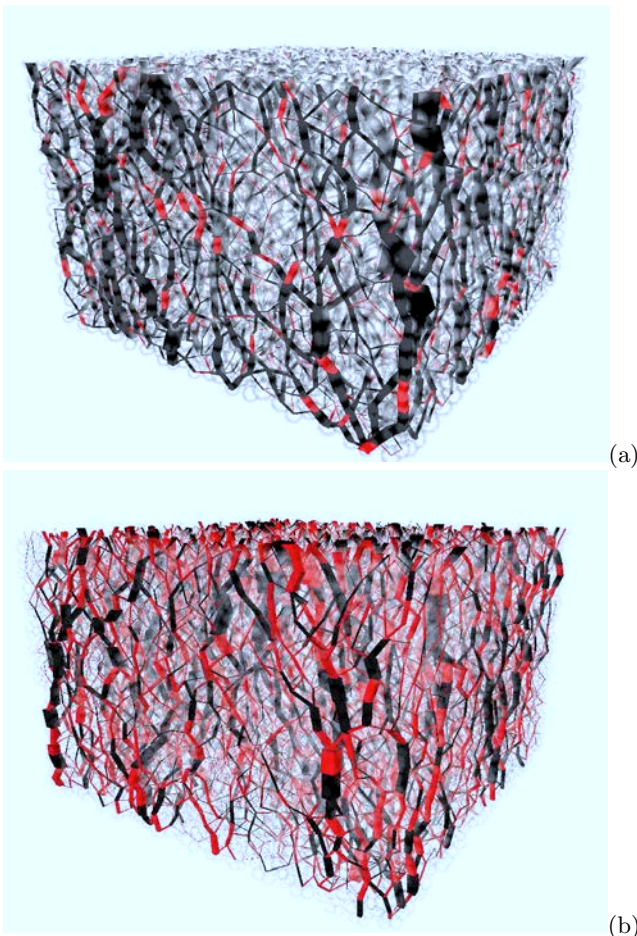


FIG. 21: (Color Online) Map of mobilized forces in red for $\eta = 0.1$ (a) and $\eta = 0.7$ (b). Line thickness is proportional to the radial force.

$(a_{\bar{t}}, \Theta_{\bar{t}}) = (a_{t'}, \theta')$ in the local neighbor frame. This function has two modes along the directions $\Theta_t \pm \pi/4$ and the ratio $a_{bart}/\bar{\mu}$ is simply their amplitude. Hence, integrating Eq. (33) in the range of $[0, \pi]$ we can define an “index” \bar{I}_{fric} for friction mobilization by:

$$\bar{I}_{fric} = \frac{5}{2\bar{\mu}} a_{\bar{t}} \quad (34)$$

The friction mobilization increases from zero in the isotropic state with shear strain and its value in the residual state depends on the nature of the material. Figure 22 shows a_t and $a_{t'}$ averaged in the residual state as a function of η . We see that a_t and $a_{t'}$ increase from 0.05 and to 0.1 and 0.3, respectively, at larger η in close correlation with the variation of S , indicating that stronger tangential and radial forces are mobilized at larger η . This is what we observe by visual inspection also in Fig.21 where two maps of radial mobilized friction forces are shown for $\eta = 0.1$ and $\eta = 0.6$ in the residual state.

The force and fabric anisotropies are very interesting descriptors of granular microstructure and force transmission properties, because they underlie the different

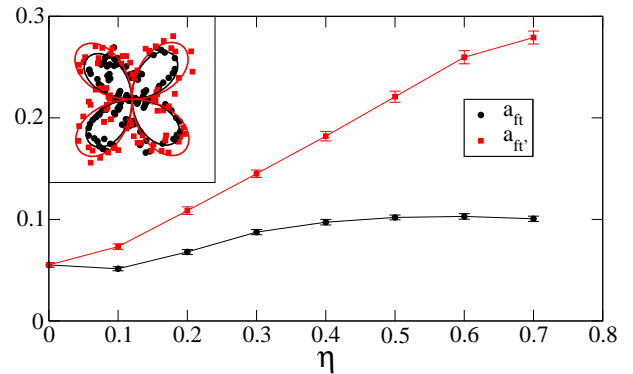


FIG. 22: (Color online) Tangential and orthoradial force anisotropies a_t (black circles) and $a_{t'}$ (red squares) as a function of η in the residual state. The error bars represent the standard deviation in the residual state. The inset shows the angular average functions $\langle f_t \rangle(\theta)$ and $\langle f_{t'} \rangle(\theta)$ in black and red, respectively, for $\eta = 0.4$ calculated from the simulation data (points) together with the harmonic approximation (lines). The error bars represent the standard deviation in the residual state.

microscopic origins of shear strength. Indeed, it can be shown that the general expression of the stress tensor (Eq.4) together with spherical harmonics approximation of the texture by Eqs. (14) and (22) and force network by Eqs. (25) and (31) leads to the following simple expression in both contact network and neighbor network frames [11, 25, 28, 58]:

$$\frac{q}{p} \simeq \begin{cases} \frac{2}{5}(a_c + a_{ln} + a_{lt} + a_{fn} + a_{ft}) & \text{(a)}, \\ \frac{2}{5}(a'_c + a_{ln'} + a_{fn'} + a_{ft'}) & \text{(b)}. \end{cases} \quad (35)$$

These expressions are based on the following assumptions, which are satisfied with a good approximation in the residual state: 1) The contact forces and branch-vector lengths are weakly correlated, 2) The reference directions coincide with the major principal stress direction: $\Theta_c = \Theta_{ln} = \theta_{lt} = \Theta_{fn} = \Theta_{ft} = \theta_\sigma$, 3) The cross products among all anisotropies are negligible. Equation (35) is based on general considerations and the values of shear strength given by this equation from the anisotropies are expected to predict correctly the measured shear strength of a packing of nonconvex aggregates, too. Note, however, that the second expression given by Eq. (35) is simpler than the first expression (four anisotropy parameters instead of five anisotropy parameters).

Figure 23 shows the normalized shear strength q/p in the residual state together with the two approximations given by Eq. (35). We see that the fit by Eq. (35)(b) is excellent for all values of η whereas Eq. (35)(a) underestimates the shear strength as particle shapes deviate more strongly from the circular shape. A similar result was reported in 3D by Ouadfel et al. [58] with ellipsoidal particles and by Azema et al. by varying the angularity of polyhedral particles [11, 28]. But the fit can be im-

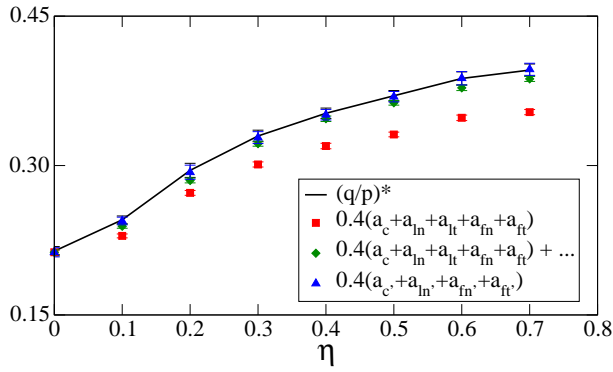


FIG. 23: (Color Online) Normalized shear stress as a function of η together with harmonic approximations given by Eqs. (35) and (36). The error bars represent the standard deviation of the data.

proved by including in Eq. (35)(a) the cross products of the anisotropies as follows [28, 58]:

$$\frac{q}{p} \simeq \frac{2}{5}(a_c + a_{ln} + a_{lt} + a_{fn} + a_{ft}) + \frac{4}{105}(a_c \cdot a_{fn} + a_c \cdot a_{ln} + a_{ln} \cdot a_{fn}) + \frac{16}{105}(a_c \cdot a_{ft} + a_c \cdot a_{lt} + a_{ln} \cdot a_{ft} + a_{lt} \cdot a_{fn}), \quad (36)$$

As we see in Fig. 23, Eq. (36) gives a better approximation of q/p than Eq. (36)(a), but is more complicated. This indicates that the analysis of the texture and force chains in terms of the neighbor network is more relevant than in terms of the contact network due precisely to the role of multiple contacts. Thus, for $\eta < 0.4$ the increase of shear strength with η can be attributed to the increase of the anisotropies and, in particular, the increase of $a_{n'}$ and $a_{t'}$ underlies the increase of shear strength at largest values of η in spite of the plateau observed for a'_c .

VI. CONCLUSIONS

In this paper, a systematic analysis of the effect of shape non-convexity on the rheological parameters of sheared granular materials was presented by means of three-dimensional contact dynamics simulations. Non-convex particle shapes are modeled as aggregates of four overlapped spheres and characterized by a single parameter η which we varied by steps of 0.1 from 0 (spheres) to ~ 0.7 . Note that an aggregate of four tangent spheres correspond to $\eta \sim 0.73$. The macroscopic and microstructural properties of several packings of 12000 aggregates under triaxial compression in a rectangular simulation cell were analyzed as a function of η .

It was shown that the shear strength in the residual state is an increasing function of η whereas the packing

fraction increases up to a maximum value before decreasing down to values comparable to that of sphere packings. It is remarkable that these two macroscopic features are shared with other nonspherical shapes described by their degree η of deviation from circular shape. This suggests that η is a “good” low-order shape parameter for describing shape effect. This finding extends also the results of a previous investigation with regular aggregates of three overlapped disks in two dimensions [36].

Another interesting feature of the aggregate packings is that their connectivity does not follow the packing fraction. Increasing nonconvexity leads to the increase of multiple contacts between aggregates with essentially the same number of neighbors per particle. This microstructural property underlies the fact that the packings are increasingly looser but with higher shear strength. As already shown for elongated and angular particles, the case of nonconvex particles illustrates again clearly that the packing fraction and its evolution are not sufficient for the description of the plastic behavior of granular media composed of non-spherical particles. The relevant internal variables as suggested by a harmonic decomposition of the stress tensor are the fabric anisotropy, normal/radial-force anisotropy and friction mobilization. A detailed analysis of the fabric and force anisotropies developed in the contact network and neighbor network frames allowed us to highlight the microscopic mechanisms leading to their observed dependence with respect to η .

The increase of shear strength stems from that of all anisotropies. Nevertheless, at higher levels of non-convexity our data indicate that the force and friction anisotropies prevail as compared to the fabric anisotropy, which tends to saturate. This saturation is related to both the increase of interlocked contacts (double and triple contacts) and the fact that the mean number of neighbors per particle remains constant. As a consequence, the aggregates can move only in the form of clusters with relative sliding and rolling localized mainly at the simple contacts leading to the increase of force and friction force anisotropies. At the same time, larger pores occur due to this “clustered” motion of the aggregates, explaining partially the decrease of packing fraction observed at higher levels of nonconvexity.

Therefore, friction mobilization and interlocking appear to play a major role at high nonconvexity and more analysis should be performed specifically for highly non-convex particles but also for other particle shapes and higher sliding friction or rolling friction between particles in order to characterize the local kinematics and clustering effects.

[1] R. Jensen, T. B. Edil, P. J. Bosscher, M. E. Plesha, and N. B. Khala, The International Journal Of Geomechanics

- [2] F. Alonso-Marroquin and H. J. Herrmann, Phys. Rev. E **66**, 021301 (2002).
- [3] S. Antony and M. Kuhn, International Journal of Solids and Structures **41**, 5863 (2004).
- [4] W. Man, A. Donev, F. Stillinger, M. Sullivan, W. Russel, D. Heeger, S. Inati, S. Torquato, and P. Chaikin, Phys. Rev. Letter pp. 198001–1, 198001–4 (2005).
- [5] E. Azéma, F. Radjaï, R. Peyroux, F. Dubois, and G. Saussine, Phys. Rev. E **74**, 031302 (2006).
- [6] I. Zuriguel, T. Mullin, and J. Rotter, Phys. Rev. Letter **98**, 028001 (2007).
- [7] A. Wouterse, S. Williams, and A. Philipse, J. Phys.: Condens. Matter **19** 406215, 14 (2007).
- [8] I. Zuriguel and T. Mullin, Proc. R. Soc. A **464**, 99 (2008).
- [9] A. Jaoshvili, A. Esakia, M. Porrati, and P. M. Chaikin, Phys. Rev. Letter **104**, 185501 (2010).
- [10] E. Azéma, F. Radjaï, R. Peyroux, V. Richefeu, and G. Saussine, Eur. Phys. J. E **26**, 327 (2008).
- [11] E. Azéma, F. Radjaï, and G. Saussine, Mechanics of Materials **41**, 721 (2009).
- [12] S. A. Galindo-Torres, F. Alonso-Marroquin, Y. C. Wang, D. Pedroso, and J. D. M. Castano, Phys. Rev. E **79**, 060301(R) (2009).
- [13] R. C. Hidalgo, I. Zuriguel, D. Maza, and I. Pagonabarraga, Phys. Rev. Letter **103**, 118001 (2009).
- [14] M. Acevedo, R. C. Hidalgo, I. Zuriguel, D. Maza, and I. Pagonabarraga, Phys. Rev. E **87**, 012202 (2013).
- [15] W. Lim and G. MacDowel, Granular Matter **7**, 19 (2005).
- [16] G. Saussine, C. Cholet, P. Gautier, F. Dubois, C. Bohatier, and J. Moreau, Comput. Methods Appl. Mech. Eng. **195**, 2841 (2006).
- [17] J. Fourcade, P. Sornay, F. Sudreau, and P. Papet, Powder Metallurgy **49**, 125 (2006).
- [18] M. Lu and G. McDowel, Granular Matter **9**, 69 (2007).
- [19] K. Maeda, H. Sakai, A. Kondo, T. Yamaguchi, M. Fukuma, and E. Nukudani, Granular Matter **12**(5), 499 (2010).
- [20] C. Noguier-Lehon, B. Cambou, and E. Vincens, Int. J. Numer. Anal. Meth. Geomech **27**, 1207 (2003).
- [21] C. Noguier-Lehon, E. Vincens, and B. Cambou, International journal of Solids and Structures **42**, 6356 (2005).
- [22] E. Azéma, F. Radjaï, R. Peyroux, and G. Saussine, Phys. Rev. E **76**, 011301 (2007).
- [23] S. A. Galindo-Torres, J. D. Munoz, and F. Alonso-Marroquin, Phys. Rev. E **82**, 056713 (2010).
- [24] E. Azéma, Y. Descantes, N. Roquet, J.-N. Roux, and F. Chevoir, Phys. Rev. E **86**, 031303 (2012).
- [25] E. Azéma and F. Radjaï, Phys. Rev. E **81**, 051304 (2010).
- [26] C. Noguier-Lehon, comptes rendus de mécanique **338**, 587 (2010).
- [27] E. Azéma, N. Estrada, and F. Radjaï, Phys. Rev. E **86**, 041301 (2012).
- [28] E. Azéma, F. Radjaï, and F. Dubois, Submitted to Phys. Rev. E (2013).
- [29] A. Donev, I. Cisse, D. Sachs, E. Vario, F. Stillinger, R. Connelly, S. Torquato, and P. Chaikin, Science **303**, 990 (2004).
- [30] A. Donev, F. Stillinger, P. Chaikin, and S. Torquato, Phys. Rev. Letter **92**, 255506 (2004).
- [31] A. Donev, R. Connelly, F. Stillinger, and S. Torquato, Phys. Rev. E **75**, 051304 (2007).
- [32] E. Nezami, Y. Hashash, D. Zaho, and J. Ghaboussi, Computers and Geotechnics **31**, 575 (2004).
- [33] E. Nezami, Y. Hashash, D. Zaho, and J. Ghaboussi, Int. J. Numer. Anal. Meth. Geomech. **30**, 783 (2006).
- [34] F. Radjaï and F. Dubois, eds., *Discrete Numerical Modeling of Granular Materials*, vol. ISBN: 978-1-84821-260-2 (Wiley-ISTE, 2011).
- [35] E. Azéma and F. Radjaï, Phys. Rev. E **85**, 031303 (2012).
- [36] B. Saint-Cyr, J.-Y. Delenne, C. Voivret, F. Radjaï, and P. Sornay, Phys. Rev. E **84**, 041302 (2011).
- [37] K. Szarf, G. Combe, and P. Villard, Powder technology **208**, 279 (2011).
- [38] Cegeo, B. Saint-Cyr, K. Szarf, C. Voivret, E. Azéma, V. Richefeu, J.-Y. Delenne, G. G. Combe, C. Noguier-Lehon, P. Villard, P. Sornay, M. Chaze, F. Radjaï, Eur. Phys. Letter p. 5 (2012).
- [39] F. Ludewig and N. Vandewalle, Phys. Rev. E **85**, 051307 (2012).
- [40] N. Estrada, E. Azéma, F. Radjaï, and A. Taboada, Phys. Rev. E **84**, 011306 (2011).
- [41] J. Moreau, Eur. J. Mech. A/Solids **13**, 93 (1994).
- [42] M. Jean, Computer Methods in Applied Mechanics and Engineering **177**, 235 (1999).
- [43] F. Radjaï and V. Richefeu, Mechanics of Materials **41**, 715 (2009).
- [44] F. Radjaï and E. Azéma, Eur. J. Env. Civil Engineering **13**/2, 203 (2009).
- [45] V. Visseq, A. Martin, D. Iceta, E. Azéma, D. Dureisseix, and P. Alart, Computational Mechanics (2012), URL [10.1007/s00466-012-0699-5](https://doi.org/10.1007/s00466-012-0699-5).
- [46] C. Voivret, F. Radjaï, J.-Y. Delenne, and M. S. E. Yousoufi, Phys. Rev. Letter **102**, 178001 (2009).
- [47] F. Radjaï, M. Jean, J. Moreau, and S. Roux, Phys. Rev. Letter **77**, 274 (1996).
- [48] L. Staron and F. Radjaï, Phys. Rev. E **72**, 1 (2005).
- [49] L. Staron, F. Radjaï, and J. Vilotte, Eur. Phys. J. E **18**, 311 (2005).
- [50] A. Taboada, K. J. Chang, F. Radjai, and F. Bouchette, Journal Of Geophysical Research **110**, 1 (2005).
- [51] N. Estrada, A. Taboada, and F. Radjaï, Phys. Rev. E **78**, 021301 (2008).
- [52] M. Botton, E. Azéma, N. Estrada, F. Radjaï, and A. Lizcano, Phys. Rev. E **87**, 032206 (2013).
- [53] C. Voivret, F. Radjaï, J.-Y. Delenne, and M. S. E. Yousoufi, Phys. Rev. E **76**, 021301 (2007).
- [54] GDR-MiDi, Eur. Phys. J. E **14**, 341 (2004).
- [55] J.-N. Roux, Phys. Rev. E **61**, 6802 (2000).
- [56] H. Troadec, F. Radjaï, S. Roux, and J.-C. Charmet, Phys. Rev. E **66**, 041305 (2002).
- [57] A. Mirghasemi, L. Rothenburg, and E. Maryas, Geotechnique **52**, N 3, 209 (2002).
- [58] H. Ouadfel and L. Rothenburg, Mechanics of Materials **33**, 201 (2001).
- [59] D. M. Mueth, H. M. Jaeger, and S. R. Nagel, Phys. Rev. E **57**, 3164 (1998).
- [60] P. T. Metzger, Phys. Rev. E **70**, 051303 (2004).
- [61] L. Silbert, Phys. Rev. E **74**, 051303 (2006).